Sinter-Based Additive Manufacturing of Graded Porous Titanium Scaffolds by Multi-Inks 3D Extrusion

Marion Coffigniez, Laurent Gremillard, X Boulnat

ADVANCED ENGINEERING MATERIALS
www.aem-journal.com

Sinter-Based Additive Manufacturing of Graded Porous Titanium Scaffolds by Multi-Inks 3D Extrusion

*Marion Coffigniez, Laurent Gremillard, and Xavier Boulnat**

A 3D printing approach to design and produce cellular scaffolds with a precise tunable pore architecture, in terms of size, fraction, and interconnectivity is reported. Different metallic inks are formulated by mixing hydrogel with Ti–6Al–4V atomized powders of various sizes. After 3D printing by direct-ink writing (DIW) followed by debinding and sintering, the fraction and size of macropores ($D > 100\,\mu m$, designed by computer-aided design (CAD)) and micropores ($D < 10\,\mu m$, remaining after sintering), the roughness and the microstructure are determined by high-resolution X-ray tomography and electron microscopy, and correlated to the initial powder size. It is shown that playing with initial powder size allows designing different pore architectures, from interconnected micropores to fully dense filaments. These phenomena are combined with a multi-inks DIW approach to fabricate architectured structures with graded microporosity. This new route is promising for the production of functional materials, such as biomedical scaffolds or implants, with tunable osseointegration, stiffness, and strength. The micropores could also be loaded with active molecules and positioned according to release needs.

1. Introduction

Tailoring the specific surface area and the porous structure of a metallic object is of great interest for many applications such as catalysis[1] or energy storage.[2] In the health sector, the introduction of porosity is a way to control the stiffness of orthopedic implants[3–5] and at the same time to improve their biological fixation through a reconstructive cellular activity made possible by vascularization.[6–8] In particular, titanium alloys, which are widely used for their biocompatibility, high specific resistance, and corrosion behavior,[9,10] are, however, criticized for being too rigid compared to bone, which leads to bone loss around the implant (stress-shielding effect).[11,12]

To counter this effect, efforts are being made to manufacture implants with controlled porosity, notably thanks to the emergence of metal additive manufacturing. Porous implants reduce their stiffness by a factor of 10–20, with Young's modulus dropping from 110 to about 10 GPa,[3,5,13] not without a notable reduction in mechanical strength. In addition, there is a growing interest in functionally graded scaffolds to better reproduce the gradient of mechanical properties of bone.[14–17] Indeed, it is important to transmit stresses in accordance with the type of tissue that receives them: cortical or cancellous bone, young or elderly patients, or patients with osteoporosis.[18,19]

Leading the way, powder bed fusion techniques, either electron beam (EB-PBF) or laser fusion (L-PBF), have demonstrated their ability to produce parts with lattice structures. Indeed, parts by L-PBF or EB-PBF can present an interconnected porosity network with a pore size usually above 300 µm,[13,20–22] which is wide enough to allow vascularization.[23] It is also common to gradually change the porosity of the structure by changing the diameter of the strut of the cell, to change its elastic modulus.[24–26] This type of pore will be called "macropores" hereafter. A significant addition of macropores often implies a reduction in strength properties. The trade-off is difficult to find, as there are a number of cases[25,26] where the yield strength obtained is lower than that of bone (130–180 MPa).[27]

As it has been shown in parallel that the presence of micropores (smaller than 100 µm) increases the volume fraction of newly formed bone,[28–32] it would seem interesting to look at the properties that can be achieved by introducing a gradient of micron-sized pores within a scaffold. This second porosity network should enhance implant anchorage, as it has been shown that there is a linear relationship between specific surface area and cell attachment.[33] However, the realization of such a structure seems to be difficult to achieve with PBF techniques. Indeed, micropores, widely documented in L-PBF,[34,35] are rather undesired defects in the context of lack of fusion on the one hand (too low beam energy density)[36,37] or the phenomenon of key-hole appearance (too high beam energy density).[38,39]

As an alternative, 3D printing processes using material extrusion, such as fused-filament fabrication (FFF) or direct-ink writing (DIW), can process feedstocks with a larger range of

M. Coffigniez, L. Gremillard, X. Boulnat
Univ Lyon
INSA Lyon
UCBL
CNRS
MATEIS
UMR 5510
69621 Villeurbanne, France
E-mail: xavier.boulnat@insa-lyon.fr

The ORCID identification number(s) for the author(s) of this article can be found under https://doi.org/10.1002/adem.202201159.

DOI: 10.1002/adem.202201159

properties, in particular in terms of the nature of the printed material and particle size. Indeed, all classes of materials can be shaped using these processes: polymers,[40,41] ceramics,[42–45] metals[46–48] and even composites,[49,50] and multi-materials.[51,52] The extruded particles can range from 20 nm[46] to over 200 µm depending on the desired resolution.[53] With these techniques, the filament produced by the extrusion of a feedstock through a thin needle is deposited according to the numeric model of the part to be printed. After printing, the parts still have to undergo thermal treatments to get rid of the organic additives and to reach acceptable densification by sintering.[54] Theoretically, these techniques can be explored to control the porosity at different scales: at least inter-filament porosity and intra-filament porosity. A careful choice of the feedstock can help control these two levels of porosity. Indeed, particle size and green density guide the sintering driving force and thus, the final pore size distribution.[55–57] One can think that coarse powders can be used to produce porous filaments after sintering, leading to a bimodal porosity in metallic scaffolds, whereas fine powders below 25 µm, as those used in metal injection molding (MIM) feedstocks, can be used to produce fully dense filaments in 3D printed parts.

As a result, the tuning of materials feedstocks could be a way to produce tailor-made porous scaffolds by material extrusion. Here, one presents an original strategy where different sizes of atomized Ti–6Al–4V powders are used to formulate different powder/binder blends as feedstocks for 3D extrusion. Using the versatile multi-material printing of such an additive manufacturing process, graded parts were produced by choosing which ink was printed on each layer. The present article shows how the initial powder influences the pore size distribution after sintering, as well as the microstructure, roughness, and mechanical properties of the obtained parts. Finally, this is applied to the production of a graded porous scaffold. This original processing route can be adapted to any sinterable metallic material to produce well-controlled functionally graded metallic parts.

2. Materials and Experimental Procedures

2.1. Fabrication Strategy

DIW or robocasting, is a four-step process consisting of: 1) formulating an ink composed of metal powders mixed with a hydrogel, 2) extruding the ink in three dimensions, 3) debinding to remove the binder before, and 4) sintering the metal powders. These different steps applied to the 3D printing of titanium scaffolds are detailed in ref.[58]. Here, we used the same strategy but applied it to different atomized powders, either printed alone or successively to produce graded structures after sintering. Each step is thus described in the following subsections.

2.1.1. Raw Powders and Inks Formulation

Ti64 argon atomized powders used in this work were purchased from TLS Technik GmbH (Germany). Two different batches with different powder size distributions were used, referred to as "coarse powder" and "fine powder" in the following. Their chemical compositions are given in **Table 1**.

Table 1. Composition of the Ti64 powders according to the supplier.

Chemical element	N	C	H	Fe	O	Al	V	Ti
Coarse powder (wt%)	0.005	0.01	<0.001	0.22	0.08	6.20	3.98	Bal.
Fine powder (wt%)	0.008	0.011	0.002	0.155	0.15	6.10	3.87	Bal.

The "Scirocco 2000" dry dispersion unit of the laser diffraction analyzer (Mastersizer 2000, Malvern Instruments Ltd, UK) was used to conduct particle size distribution (PSD) measurements on the as-received Ti64 powders. Three measurements, presented in **Figure 1**, were performed on each powder, using 2.611 as a refractive index value.

According to the laser diffraction results, both powders present a monomodal size distribution. Ti64 particle diameters of the fine powder range between 0.4 and 7 µm, while those of coarse powders extend from 2 to 70 µm. PSD of coarse powder is, therefore, far larger than the one of fine powder. Distributions are characterized as follows: $D_{10} = (2.93 \pm 0.02)\,\mu m$, $D_{50} = (4.31 \pm 0.07)\,\mu m$, and $D_{90} = (5.83 \pm 0.07)\,\mu m$ for the fine powder, and $D_{10} = (11.6 \pm 0.02)\,\mu m$, $D_{50} = (23.1 \pm 0.01)\,\mu m$, and $D_{90} = (37.2 \pm 0.04)\,\mu m$ for the coarse powder.

Here, we used the two types of atomized titanium powders, and a mix of them, as raw material for ink formulation.

To be extrudable through a fine nozzle under a reasonable pressure, an ink should present a shear-thinning behavior. However, as explained by M'Barki et al., it should also present a sufficiently high dynamic yield strength to compensate for both capillary forces and gravity.[59] This would give the ink the ability to retain its shape straight after printing, and support the subsequent layers. A detailed study of the rheological behavior obtained by varying the Ti64 ink formulation is given in ref. [58].

In the present study, the inks were composed of Ti64 atomized powders dispersed in a Pluronic F-127-based hydrogel

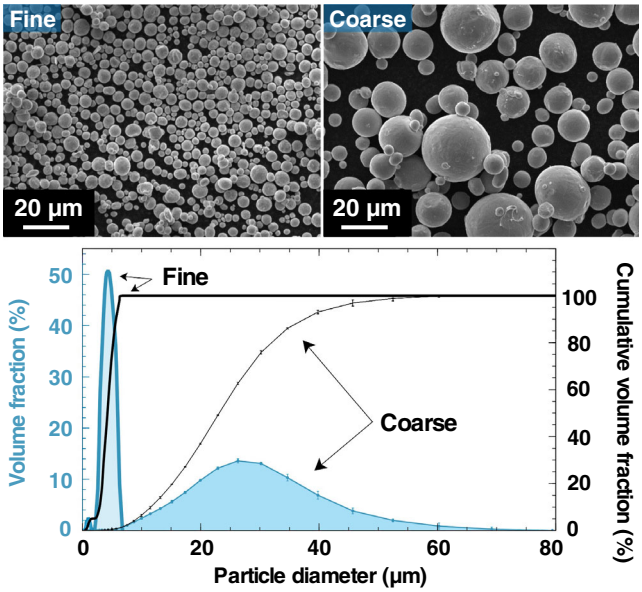

Figure 1. Scanning electron microscope (SEM) images (secondary electrons) and particle size distributions (PSDs) of the two gas-atomized powders used in this study.

Table 2. Inks composition and nomenclature.

Name	Powder solids loading in the ink
Fine50	Fine 50 vol%
Coarse50	Coarse 50 vol%
Mix50	(70% Coarse + 30% Fine) 50 vol%

binder. The Pluronic F-127 is a poly(ethylene oxide)–poly(propylene oxide)–poly(ethylene oxide) triblock co-polymer (furnished by Sigma Aldrich), and when dissolved in water it has the interesting property to form temperature-sensitive gels: liquid-like at low temperature (near 0 °C), solid-like at room temperature. It was used here in the form of dried granules for the binder preparation, gradually dissolved in de-ionized water to form a 25 wt% hydrogel. For each ink, Ti64 addition was performed in three steps. The batches were mixed in a dual asymmetric centrifugal mixer (SpeedMixer DAC 150.1 FVZ-K) for 1 min at 1500, 1700, and 2000 rpm after the first, the second, and the last addition, respectively. Prior to each mixing step, inks were kept for 10 min at 4 °C to be mixed in a liquid state.

The nomenclature provided in **Table 2** is used to identify the studied inks.

2.1.2. 3D Printing by DIW

The three resulting inks were first printed separately and then successively to form the same sample together.

Printing was performed using a commercially available robocaster (3D Inks LLC, Tulsa, OK, USA), controlled by the motion software Aerotech A3200 (Aerotech Inc., Pittsburgh, PA, USA). Samples were printed on glass plates, and wetted with a thin layer of grease for easier dried samples removal. Inks were extruded through conical nozzles presenting an internal diameter of 840 μm using a printing-head speed of 10 mm s^{-1}. The rod spacing was fixed at 1.260 mm, which corresponds to 1.5 times the internal diameter of the nozzle. In addition, the space between two successive layers was fixed at 0.8 times the internal diameter of the nozzle, to ensure a slight interpenetration without crushing the filaments.[60] This geometry leads to a relative density of 67.86%, assuming fully dense struts. To ensure a stabilized flow during scaffold printing, a few sacrificial millimeters of ink was extruded prior to printing each sample. In addition, the temperature was maintained at 25 °C in the printing chamber.

For the graded parts, as the robocaster included several syringe holders, the three inks were successively printed through three different syringes to form a single scaffold.

2.1.3. Debinding and Sintering

Printed scaffolds were dried for 48 h at an ambient temperature above 22 °C before being removed from the glass substrate. They were then thermally debinded and sintered, using a Nabertherm N 11 h^{-1} furnace equipped with an in-house setup enabling a controlled atmosphere. As presented in a former work,[58] the debinding treatment was chosen based on thermogravimetric analysis: 1) a heating rate of 1 °C min^{-1} from room temperature to 350 °C, 2) 30 min at 350 °C, and 3) a cooling rate of 1 °C min^{-1}. This whole debinding process was completed under a primary dynamic vacuum (around 5×10^{-2} mbar).

Finally, samples were sintered for 2 h at 1200 °C, using a heating rate of 10 °C min^{-1} and the natural cooling rate of the furnace. This latter decreases from 20 °C min^{-1} to less than 1 °C min^{-1} as the temperature drops. This sintering step was carried out under a dynamic secondary vacuum (below 5×10^{-4} mbar).

2.2. Characterization

2.2.1. SEM Analysis

Images of powders and structures were acquired in a Tescan Vega3 scanning electron microscope (SEM) equipped with a tungsten filament (Tescan Orsay Holding, a.s., Brno, Czech Republic). Both secondary electrons (SE) and backscattered electrons (BSE) modes were used.

Electron backscatter diffraction (EBSD) map acquisitions were performed in an SEM Zeiss Supra 55 VP with a field-emission gun, using an Oxford Instrument EBSD Symmetry camera. EBSD map acquisitions were performed at an acceleration voltage of 20 kV, with an aperture size of 120 μm, using the high current mode. A step size of 200 nm was sufficient to well detect the β phase. EBSD maps were post-treated with Channel 5 software, and a 5° grain boundary criterion was applied to calculate the mean grain size.

2.2.2. Structure Analyses Through X-ray Tomography

Sintered scaffolds were analyzed by X-ray computed tomography using a V|tome|x tomograph (GE Sensing & Inspection Technologies Phoenix X-ray GmbH, Boston, MA, USA) (100 kV X-ray tube voltage, 0.1 mm Cu filter, 1200 projections over 360° rotation, three images per projection, 667 ms of exposure time, and 8 μm of voxel size). In addition, sintered monofilaments were imaged at higher resolution in an EasyTom Nano tomograph (RX Solutions, Chavanod, France) (100 kV X-ray tube voltage, 1248 projections over a 360° rotation, three images per projection, 4 s exposure time, and 0.45 μm voxel size). In both cases, 3D volumes were reconstructed from the gathered radiographs by applying a filtered back projection Feldkamp algorithm. Images analysis was then conducted with the free and open-source Fiji software.[61]

X-ray tomographic scans of sintered scaffolds and filaments were used to determine both shrinkage and density. Indeed, as more detailed in a previous work,[58] image analysis enables obtaining the enveloping outer shell of the structure for each plan of observation. The dimensions of the latter can thus be measured with pixel accuracy (0.45 μm). Size measurements obtained by this technique were then compared with CAD dimensions (given as an input to the robocaster) to obtain process shrinkage. In addition, scanned scaffolds were also weighed and each mass obtained was divided by the corresponding scaffold volume to get their density. The Ti64 density considered to determine the scaffolds relative density was 4.43 g cm^{-3}.

Pores within filaments were quantified and characterized using X-ray tomographic scans of filaments and the same image

analysis procedure as described in a precedent study.[58] To avoid having measurements influenced by noise, only pores containing more than eight voxels were kept for characterizations. This means that only pores with sides larger than 0.9 µm are detected in this study.

2.2.3. Roughness

Two different techniques were used to perform filament surface roughness measurements. The first approach was to use X-ray tomography scans of single constitutive filaments and extract 36 lines along the height of the filaments (1 line every 10°), using the radial reslice tool as explained in Persenot et al. work.[62] Additional measurements were performed along the outside filaments of a graded scaffold using a Hirox Nano Point Scanner–White Light Confocal system. With this second technique, acquisitions were performed along a surface and not only a line. Beyond local sequences of peaks and valleys, surfaces may also present waviness patterns that should be removed to avoid distortion of the measurement. These waviness patterns are at much lower frequencies than roughness (they represent larger elements) and are therefore eliminated using high-pass filters. No tilt correction was necessary for the surfaces analyzed in this study, however, a Gaussian filter with a wavelength of 0.8 mm was used to suppress the wave effect.

The parameters commonly used to quantify linear roughness are defined by the IS0 4287 standard as follows: R_a, R_p, R_v, R_z, are the arithmetic mean roughness, the maximum peak height, the maximum depth of the valleys, and the maximum profile height, respectively, with $R_z = R_p + R_v$.

All these parameters for representing the roughness obtained along a line can be extended to surface analysis. They are then referred to as S_a, S_p, S_v, and S_z, respectively, according to the ISO standard 25178.

2.2.4. Interstitial Content

Carbon and oxygen contents, respectively, were measured by combustion method, using a CO_2 nondispersive infrared (NDIR) detector and a nondispersive infrared CO cell, respectively. Details of the procedures are given in previous work.[63]

2.2.5. Mechanical Testing

Vickers hardness tests were carried out on previously polished cross-sections which were perpendicular to the building direction. A 500 gf load was applied and the average value for each sample was calculated over more than ten measurements.

Compressive tests were conducted on approximately cubic scaffolds, using an Instron 8502 universal testing machine, equipped with a 100 kN load cell. A preload of 100 N was first applied, followed by a 0.05 min^{-1} strain rate. As it is recommended to have at least seven times the foam cell size in each direction to prevent size effect,[64] tests were performed on samples consisting of 18 layers containing 10 struts each ($\approx 10.2 - 10.3$ mm side after sintering). Top and bottom surfaces were polished prior to tests, to ensure that the surfaces were flat and parallel. A machine stiffness correction was applied according to the measurement performed on a sample with a known stiffness (a piece of 2017 A at T4, presenting Young's modulus of 74 GPa). Surface damage was followed by filming one side of the sample during the test with a mvBlueFox camera. In addition, one compression test per specimen type was interrupted at different loads to allow 3D damage assessment by X-ray tomography. These scans were also used to plot strain maps by performing digital volume correlation (DVC), for which further details are given in Appendix B.

In addition, three-point bending tests were performed on 10 constitutive filaments of each ink. Tests consisted of a preload of 0.2 N, followed by a loading rate of 0.05N.s^{-1}. They were conducted using an Electroforce 3200 test machine (Bose, Eden Prairie, MN) equipped with a 22 N load cell. The length between the two support points was fixed at 10 mm. Since the cross-section could slightly differ from one filament to another and was not always exactly circular, the effective cross-section of each fractured sample was measured using an RH-2000 microscope (Hirox). Analyses of these images then enable access to the barycentre (which will give the position of the neutral axis) and the quadratic moment of each fracture surface, meaning that the calculations were performed at the point of rupture. It was then possible to plot stress–strain curves for each sample considering the following relations

$$\sigma = \frac{FL}{4I}\gamma \tag{1}$$

and

$$\varepsilon = \frac{6D\gamma}{L^2} \tag{2}$$

with F the force applied on the sample, L the distance between support points, I the quadratic moment, γ the distance to the neutral axis, and D the deflection.

3. Results and Discussion

3.1. Densification and Shrinkage

Figure 2 shows examples of scaffold structures in their as-printed ((a) and (b)) and their as-sintered ((c) to (f)) states. It should be noted that scarce but large pores can sometimes be observed within filaments of samples printed with the ink containing 100% of fine powder, as revealed by the SEM image presented in Figure 2c. This is the result of air bubbles trapped in the ink when it is mixed, and kept despite the printing stage. This problem could be avoided by carrying out the mixing steps under vacuum and by using a dedicated transfer system to convey the ink into the syringe.

In addition, both filament cross-sections of the three types of inks displayed here, and the X-ray tomographic sections presented in **Figure 3** underline the significant effect of the powder size on the density obtained. Indeed, decreasing the particles' mean diameter from 23 to 4.3 µm enables to decrease the remaining porosity within filaments from 12.5% to 0.025%. The use of the powder blend leads to an improvement in densification compared to coarse powder but not compared to a fine powder (remaining porosity of 4.4%).

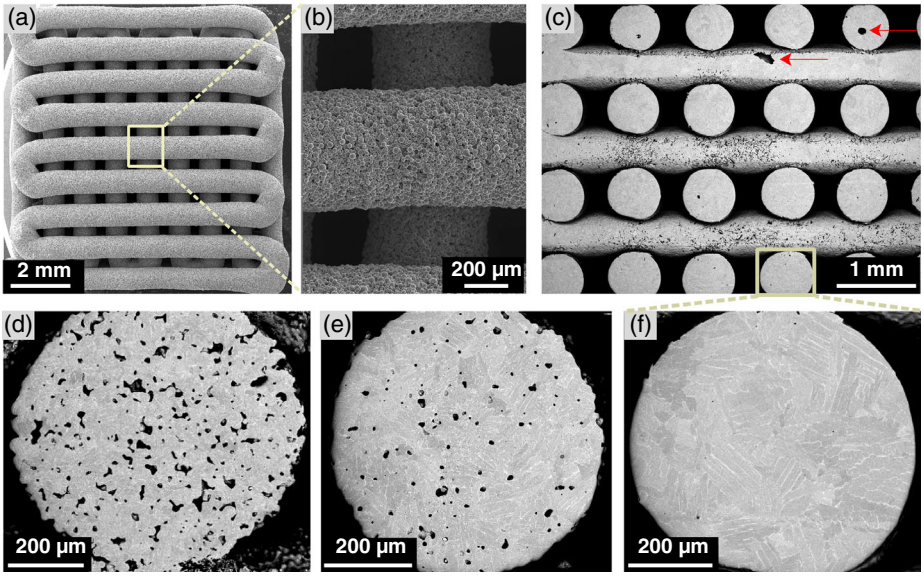

Figure 2. a) SEM image of a dried 3D printed Ti–6A–4 V scaffold made from Coarse50 ink, b) with a zoom on a constitutive filament. c) View of a cross-section obtained for a sintered scaffold made with fine powder only. Red arrows highlight the fact that air bubbles trapped in the ink during mixing can be retained after sintering in the case of samples completely made from fine powder. Intrafilament sintered powders are drawing either fully dense filaments or micro-sized pores depending on the powder size: d) coarse powder only, e) powder blend, and f) fine powder only.

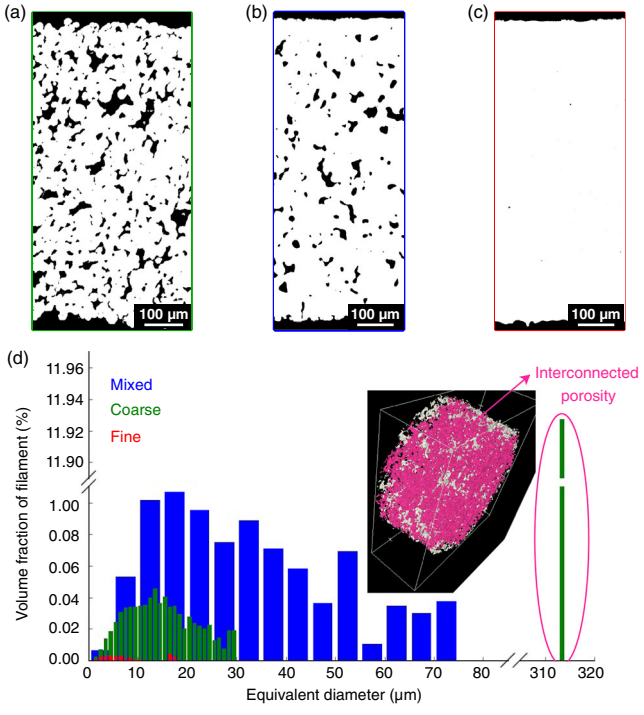

Figure 3. Remaining porosity after sintering: Example of a tomographic section of sintered filament containing: a) coarse powder only; b) the two mixed powders; c) fine powder only. d) pores volume distribution for the three powder batches. A 3D reconstruction of pores within a filament made from coarse powder is given to highlight the presence of an interconnected porosity network as the larger pore plotted in pink is present in the whole height.

Bimodal particles size distributions are usually used as they enable to reach higher green density, as shown by German et al.[55] However, with processes such as robocasting, particle rearrangement that takes place during drying and debinding steps probably does not lead to the most optimal stacking. In addition, a higher green density obtained through bimodal distribution does not necessarily lead to an increase in post-sintering density. This intermediate effect observed here, with the improvement compared to the 100% coarse powder case but a decrease in density compared to the 100% fine powder case has already been observed as shown in a more recent work by German et al.[65] Two factors may explain this lower density than with fine powder. The first one is the decrease in coordination number (number of neighboring particles to a given particle) caused by the addition of large-size powder, which decreases the sintering driving force.[65] The second reason is related to the faster densification of fine particles (compared to coarse ones). This difference in densification rate results in a constrained shrinkage for small particles powder near large particles. This is reflected in the presence of large residual pores near large particles. In addition to this global remaining porosity evolution, pore size distributions shown in Figure 3d highlight the closure of the interconnected pores network for the two samples containing fine powder. Indeed, the distribution of pores within the filament made from coarse powder presents one very large pore which occupies a volume identical to that of a sphere of 314 µm in diameter, in addition to small pores with an equivalent diameter below 30 µm. On the 3D reconstruction given as an illustration of coarse filament pores, the larger pore has been represented in pink and all the other ones in white. It can be clearly seen that this larger pore is present within the whole analyzed sample and is thus an interconnected open porosity. This sample is thus in the second sintering stage, for which not only neck

formation but also consequent densification (from 50% to 87%) occurred, but without closing the interconnected porosity. On the opposite, samples made from mixed and fine powders do not present one large pore that remains present all along the filament. These two samples are thus in their final sintering stage according to Kang (isolated pores only), which is also in agreement with the remaining percentage of porosity being below 7% for both samples.[66] However, the filaments made from the powder blend present a larger volume of closed porosity, made of larger pores than the two others, due to the constrained shrinkage mentioned earlier.

The observed differences in densification are also accompanied by varying shrinkages, as described in **Table 3**.

Contrary to what is observed on samples of higher porosity, the shrinkage seems to lose isotropy with the addition of fine powder. For the blend and the fine powder, the shrinkage in the stacking direction of the layers is lower than those in the layer deposition plane. In view of the feeling when printing these different inks, it is thought to be linked to an increase in ink stiffness with the addition of fine powder, which prevents the interpenetration of the layers required by the CAD from being respected. Indeed, the same CAD file was used for the three inks, asking for a distance of 672 µm between two layers, but the interpenetration seen by both SEM and X-ray tomography seems to differ depending on the ink used as it can be seen in Appendix A.

3.2. Roughness

The difference in roughness induced by the different powders batches can be visualized on the 3D reconstructions of the volumes acquired by high-resolution X-ray tomography presented in **Figure 4**. For measurements performed with the Hirox Nano Point Scanner–White Light Confocal system, linear values were taken along the lines separating the analyzed surfaces into two halves. Profiles obtained along these lines are shown in Figure 4. The dark red line on each of the graphs represents the wave pattern that has been subtracted from the profile to obtain the values. All the results obtained with the two techniques are gathered in **Table 4**. Note that it was not possible to measure the roughness of samples made from coarse powder using the technique relying on X-ray tomography scans. Indeed, as these samples present an open interconnected porous network, the boundary between what should be considered as roughness and what should be considered as porosity would then have to be defined in a totally arbitrary way, meaning that any kind of results could have been obtained. The authors, therefore, preferred to consider that this method was not relevant for measurements on a sample with open and interconnected porosity.

Roughness is considerably decreased with the use of fine powder leading to almost full densification. Also, it should be noted that linear measurements tend to underestimate the different values compared to surface measurements, simply because of the smaller area of analysis they represent. The same effect is obtained with measurements performed on X-ray tomographic scans due to the smaller length analyzed (585 versus 3880 µm for filaments made with the powder blend). Despite this underestimation, linear measurements are still widely used and are therefore interesting for comparisons.

It may be worth noting that the intrafilament roughness obtained by DIW in this study is lower than that obtained by both electron beam and laser beam PBF even in the case of interconnected residual porosity. Indeed, considering values obtained for constitutive struts of Ti64 porous structures, it appears that as-built LPBF parts can present R_a between 10 and 15 µm.[67–69] Parts obtained by EB-PBF present even slightly higher values (R_a between 30 and 45 µm and R_v around 200 µm), as shown by Persenot's measurements along constitutive struts of a porous structure.[70] Note that keeping a low roughness can be interesting for fatigue resistance properties.[70] However, the quantification presented here concerns only the roughness of the filament themselves. But in the case of dense part production by DIW, one should also be interested in the inter-filament roughness (between layers).

Table 3. Process shrinkage and relative density obtained for the different powder size distributions used.

Powder used	Shrinkage [%]				Relative density [%]	
	Along *X*	Along *Y*	Along *Z*	Volume	Measured	Designed[a)]
Coarse	15.3 ± 0.3	15.3 ± 0.4	15.2 ± 0.3	39.2 ± 0.3	57.3 ± 1.0	59.38
Mixed	16.3 ± 0.3	16.2 ± 0.2	15.3 ± 0.4	40.7 ± 0.6	60, 0 ± 0.4	62.84
Fine	18.6 ± 0.2	18.5 ± 0.2	17.0 ± 0.3	44.8 ± 0.2	63.5 ± 0.6	67.84

[a)]Calculated considering CAD design but also remaining porosity within struts.

3.3. Microstructure

3.3.1. Homogeneous Scaffolds

To complete structural analysis, sample microstructures were investigated through EBSD analysis as shown in **Figure 5**.

All three types of samples have a similar grain morphology, presenting thick unclosed lamellae. Of the ≈300 grains analyzed for each case, no major changes in terms of the proportion of phases are to be reported, but only a moderate increase in α grain size for samples containing fine powder. This might be due to a higher oxygen content reached by fine powder, oxygen stabilizing the α phase. Indeed, according to the TTTI3 thermodynamic database,[71] β transus is shifted from 942 °C for a sample containing 0.2 wt% of oxygen as with the coarse powder, to 1050 °C for a sample containing 1 wt% of oxygen which is the order of magnitude measured for samples made of fine powder. In addition, pores can also impede grain growth. So the fastest densification obtained with fine powder can enable a more important crystal growth.

The difference presented here in terms of density and roughness is obtained for a single sintering temperature meaning that obtaining a material with an intra-filament porosity gradient could be considered.

3.3.2. Graded Scaffold

A polished cross-section of an as-sintered scaffold with a density gradient is presented in **Figure 6**. This scaffold is composed of

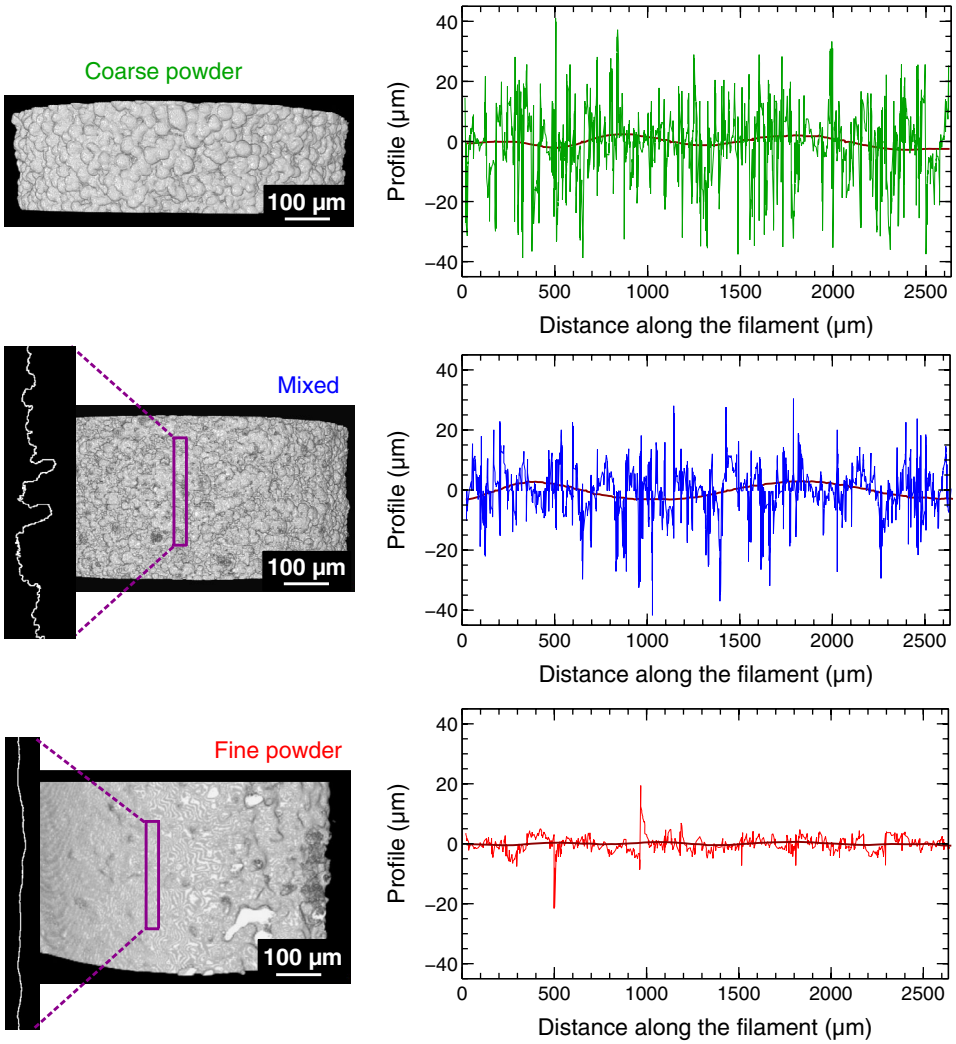

Figure 4. Linear roughness profiles obtain the following struts made from each powder batch with associated 3D reconstructions from X-ray tomography showing surface aspect.

Table 4. Surface and linear roughness measured by both X-ray tomography with the Hirox Nano Point Scanner–White Light Confocal system. All the roughness values are in micrometers. The investigated areas are also given.

Powder used	Area [µm²]	Hirox Nano Point Scanner							X-ray tomography			
		S_a	S_p	S_v	S_z	R_a	R_v	R_z	Length	R_a	R_v	R_z
Coarse	289 × 2636	9.86	63.0	41.0	104	9.65	38.0	75.5	N.A	N.A	N.A	N.A
Mixed	225 × 3880	8.02	40.0	58.2	98.2	6.43	36.8	63.5	585	4.5	14.0	33.3
Fine	176 × 3246	2.54	25.3	30.4	55.6	1.94	11.8	23.0	555	1.6	8.8	14.4

12 layers: the first four ones are made from an ink obtained from the fine powder, the four subsequent ones from the two mixed powders, and the top ones from a coarse powder only. Particular attention had to be paid to the alignment of the different syringes to avoid the formation of a misalignment when changing the ink.

Despite the difference in shrinkage between each ink, no crack formation was observed by X-ray tomography. However, the filaments of the ink with the highest shrinkage show a curvature probably related to the stresses exerted by this difference in shrinkage. This type of deformation could be avoided by adding intermediate cases. Gradual mixing can even be envisaged using

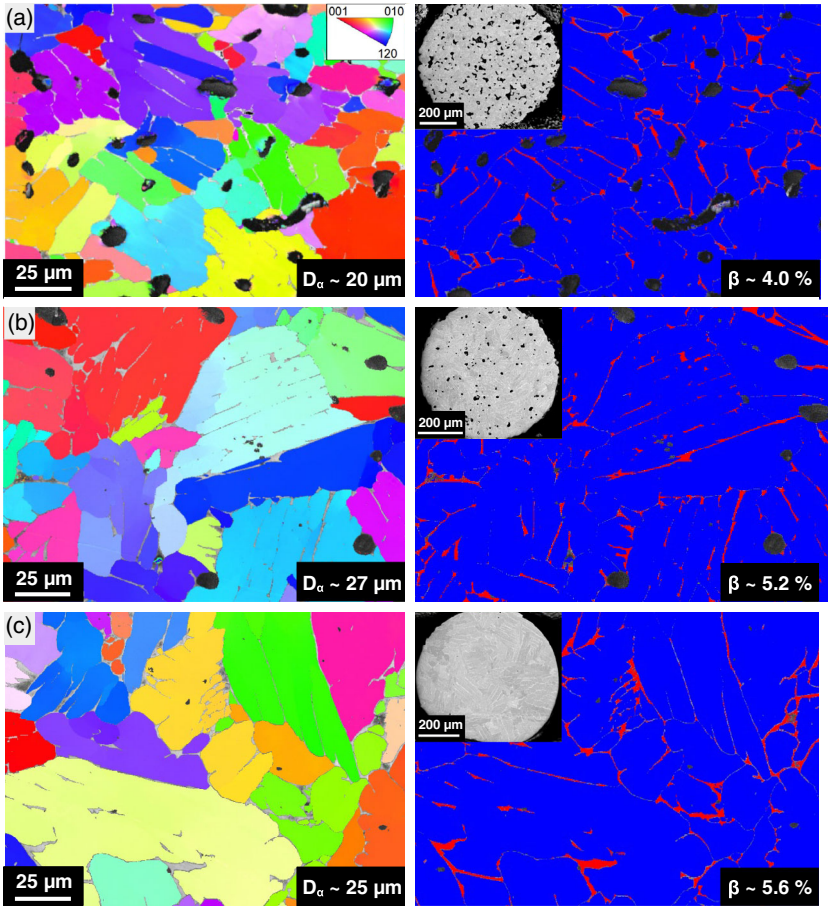

Figure 5. Microstructure evolution with powder size: EBSD IPF maps and their associated maps of phase for sintered samples made of: a) coarse powder only; b) the two mixed powders; c) fine powder only.

systems such as an ink mixer directly feeding the nozzle as proposed by ref. [51].

3.4. Mechanical Properties

3.4.1. Intrinsic Filament Properties

First, to access the intrinsic properties of the constitutive filaments, three points bending tests and Vickers hardness were performed on filaments made from the three powder batches. **Figure 7** shows the results obtained with the three points bending tests. It can be seen that filaments Young's moduli are increasing with their density. Filaments presenting 12–13% of porosity show Young's moduli around 62 GPa which is in agreement with previous studies on porous titanium.[72,73] However, values a little bit above the bulk reference are reached with the filaments made of fine powders only (120 GPa against 110 for the bulk reference).[73] In addition, the densification is also accompanied by a loss of ductility. These results could be attributed to an increase in oxygen content owing to the greater specific surface area of the fine particles. To verify this hypothesis, carbon and oxygen contents were also measured on samples from the blend and the fine powder batches. No real consequences of the powder size were observed on the carbon uptake, with a final amount kept at 0.1 wt% (against 0.094 wt% previously found for samples made from coarse powder). However, oxygen uptake was far larger, even higher than the one observed in samples obtained with a non-optimized debinding treatment.[63] The oxygen uptake along the whole process was indeed evaluated at roughly 8500 ppm (+ 0.85 wt% between the initial and the final state) for the fine powder, against 1000 ppm (0.1 wt%) for the coarse. This leads to the final oxygen content of 0.220 wt% in samples completely made from a coarse powder only, against 1.2–1.3 wt% in samples containing only fine powder. A similar influence of powder size on oxygen uptake had already been observed for the MIM process.[74] It would then be necessary to increase precautions to limit oxygen intake when using fine powder.

In addition, Vickers hardness increases with the filament density as shown in **Table 5**. However, the observed trend is not only due to the increase in density but also to the increase in oxygen content. Considering that adding 1 wt% of oxygen in Ti64 leads to a 70 Hv increase in hardness as shown by Zabler et al.,[75] the contribution of densification obtained by going from coarse to fine powder can therefore be estimated at about 100 Hv. It should also be noted that a larger scatter for the samples produced with the powder mixture is observed here.

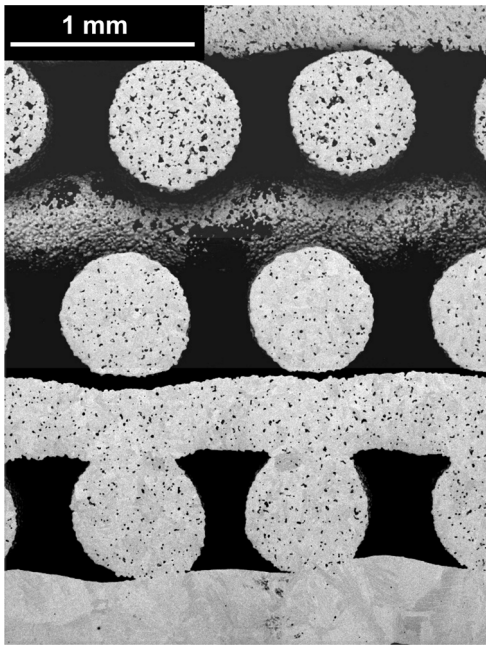

Figure 6. SEM image of a scaffold presenting graded microporosity (within filaments).

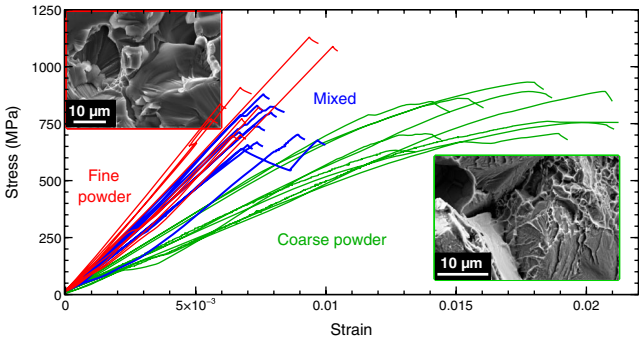

Figure 7. Stress–strain curves obtained by three-point bending on filaments and illustrated with fracture surfaces. Samples containing fine powders show brittle fracture surfaces (cleavage) whereas dimples can be found on a sample containing coarse powder only.

Table 5. Vickers hardness and Young's moduli of constitutive filaments depending on the ink used.

Ink used	Hardness [Hv]	Young's modulus [GPa]	E/ρ
Coarse50	243 ± 8	62 ± 8	15.5
Mix50	325 ± 17	104 ± 8	24.5
Fine50	410 ± 8	121 ± 7	28.0

3.4.2. Scaffolds Properties

Figure 8a shows the compressive curves obtained for samples from the three powder batches. The expected improvement in yield stress with density was indeed observed with an increase from 265 MPa for scaffolds made with coarse powder to 425 MPa for scaffolds containing only fine powder. In addition, a slight increase in scaffolds apparent Young's modulus is observed with the addition of fine powder. Indeed, according to the curves, this value increases from 28–30 GPa for scaffolds made of coarse powder to 35–45 GPa for scaffolds obtained using the mixed powder batch and to 55 GPa for scaffolds containing only fine powder. Note that both yield stresses and apparent Young's moduli of scaffolds made from the mixed powders seem again more scattered even though additional statistics are required to confirm this observation. This could be due to a difference in the ratio of the two powders between the two scaffolds. Interestingly also, the ratio of the average apparent modulus of the densest scaffolds to that of the most porous ones is $55/29 = 1.9$. This stays similar to the ratio of the average modulus of the dense filaments to that of the most porous ones (1.95), even though the difference in density is less important for scaffold than for filaments ($63.5 - 57.3 = 6.2\%$ for the scaffolds against 12.5% for the filaments). It thus seems that the constitutive filaments' properties are preponderant in the behavior of whole scaffolds.

This improvement in strength is also accompanied by a loss of ductility. Indeed, a crack propagating at 45° to the direction of compression appears for strains between 5% and 10% in the case of samples containing fine powder (partially or totally). X-ray tomography analysis confirmed that this crack does indeed damage the entire sample as shown in Figure 8a. Slipping of one half of the specimen relative to the other occurs along this crack. This behavior is similar to what has been previously observed for samples debinded at 500°,[63] for which a high equivalent oxygen content led to a low ductility. In the case of samples containing only coarse powder, a crack at 45° might appear in a corner (it has been observed only in one sample) but is not able to cross the whole sample. The loss of ductility observed in samples containing fine powder can therefore be directly related to the more brittle character of their constitutive filaments, due to their higher oxygen enrichment.

From a macroscopic mechanical point of view, the graded sample shows the aforementioned weak points of each layer: a yield strength identical to that of the most porous layers and the low ductility of layers containing fine powder (due to higher oxygen content). However, it should be considered that the strain is likely to be non-homogeneous in these samples, as highlighted by the height reduction of the different layers, which increases with the decrease of filament density (see Figure 8b,c). The most porous layers thus begin to densify at a stress level similar to that which triggers the densification of scaffolds of the same porosity. Finally, the first damage of this graded structure is located in the layers made with the powder mixture and at the interface between these layers and those obtained with the fine powder. Both the measured difference in height reduction and the damage localization are in agreement with the map of strain obtained by DVC and given in supplementary materials. All the steps for which the convergence of the DVC calculation has been obtained are shown in Figure B1. The further stage, after the last one presented at the bottom, led to the formation of the crack at 45° visible in Figure 8c. This crack formation prevented the success of the correlation for this stage. The location of this damage might be explained by the fact that layers

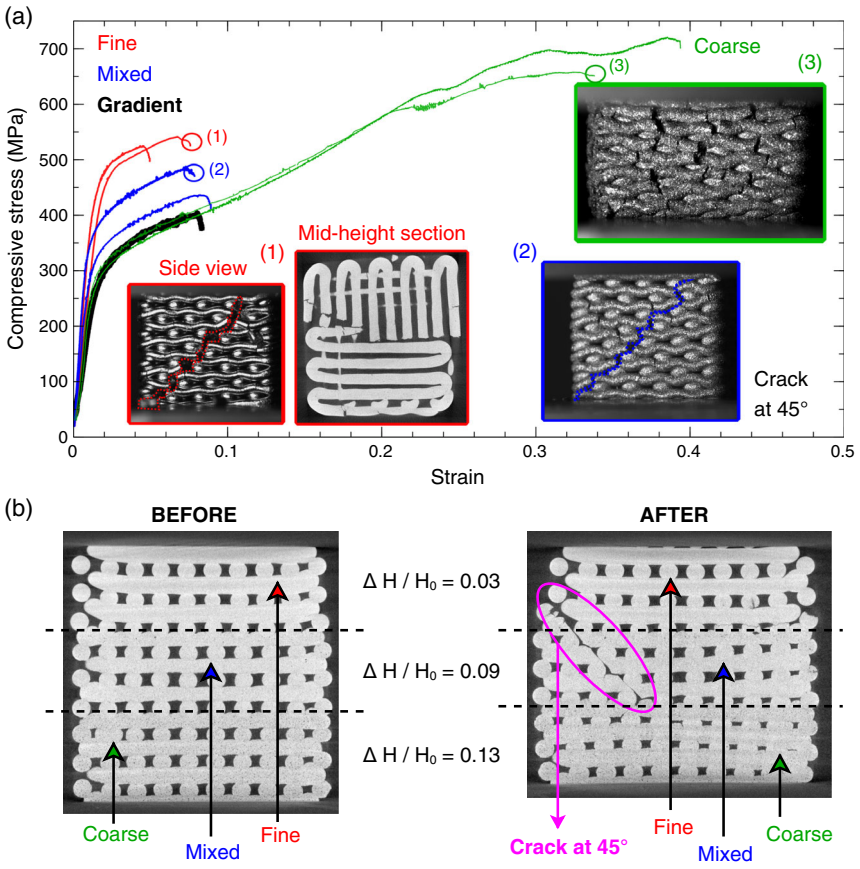

Figure 8. Effect of powder size on scaffold mechanical properties: a) stress–strain curves obtained under compression and illustrated with scaffold structures at the end of tests. b) X-ray tomographic sections of the gradient scaffold before and c) after the compressive test showing the height evolution for the different kinds of layers.

made with the powder mixture are the only ones that are constrained both above and below by layers with a different shrinkage from their own. Producing a more gradual gradient would then probably be beneficial to avoid preferential damage to the layers most stressed by the difference in shrinkage. However, it should be noted that this damage occurs at a similar level of strain to those achieved by scaffolds containing fine powder (100% or mixed).

4. Conclusion

For the first time, this study shows the feasibility to produce scaffold structures presenting a gradient of porosity at the micron scale, by varying the size of the extruded powder. Indeed, as this parameter influences the sintering kinetics, the different powders do not reach the same densification stage for the same sintering treatment. As shown in this study it opens up a wide field of possibilities: 1) The roughness from coarse to fine powders can be decreased almost fivefold, from the roughness range of L-PBF to an average roughness of around 2 µm, which could be of interest for fatigue properties. 2) It is possible to go from filaments presenting an open and interconnected porosity network to almost fully dense filaments using a single set of sintering parameters. 3) As a consequence, mechanical properties can thus be tuned in terms of both hardness and yield stress, with only a reasonable effect on scaffold Young's modulus. This could therefore be an alternative to varying the filament thickness (and thus the distance between filaments) to adapt the mechanical properties. However attention should be paid to the oxygen enrichment that comes with the use of smaller powders and which can embrittle the structures. 4) This processing route could allow tunable osseointegration of metallic implants or scaffolds. Be able to choose the microporosity location could also be a way to load these scaffolds with active molecules where needed.

Appendix A

Layers Overlap Evolution

Regardless of the inks used in this study, the distance between the two layers was set at 0.8 times the needle diameter to ensure good adhesion between layers. However, the structure obtained with the fine powder gives the illusion that no covering was required. This may be related to a greater stiffness of the ink made from the fine powder (**Figure A1**).

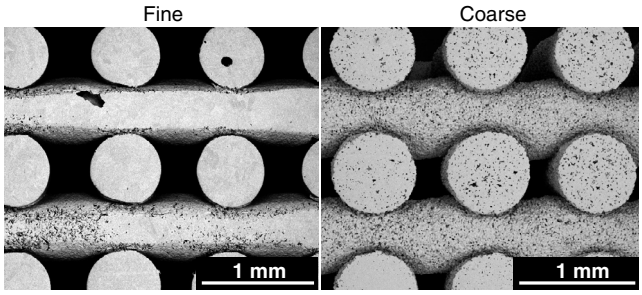

Figure A1. Layers overlap: SEM images of samples printed with inks containing fine powder (left) and coarse powder (right). The overlap between layers of the sample with coarse powder is more important than the one of the samples with fine powder.

Appendix B

Digital Volume Correlation

The purpose of correlating digital images (or volumes) is to digitally reconstruct the field of movement that describes the evolution of the reference image toward the distorted image. To do so, the whole region of interest (ROI) must be divided into sub-images (or sub-volumes) identifiable by a unique grayscale pattern. The optical flow equation Equation (B1) then allows to consider that the variations of the gray levels between the two images are only due to the displacement of the material points.

$$f(x) = g(x + \mathbf{u}(x)) \tag{B1}$$

where f corresponds to the reference ROI and g to the distorted ROI, x is the vector giving the current point position (with respect to the ROI coordinate system) and $\mathbf{u}$ the unknown displacement vector field.

The method of least squares is then used to solve this problem. The technique consists of minimizing, by taking into account a displacement $\mathbf{u}$, the following residue

$$\varphi_c^2(\mathbf{u}) = \frac{1}{2}\iiint_{\mathrm{ROI}} [f(x) - g(x + \mathbf{u}(x))]^2 \mathrm{d}x \tag{B2}$$

Since the residue is dependent on $\mathbf{u}$ in a nonlinear way, the resolution method consists in solving this problem iteratively by displacement increments d$\mathbf{u}$. To find more details on the resolution method, please refer to Chapter 3 of Lachambre's thesis.[76] The criteria for validating the solution over a number of iterations are

Error stabilization $\varphi_c^2\ (\mathbf{u}) \to \varepsilon$.

Convergence of the displacement increment d$\mathbf{u}$ toward 0.

If the difference between the two images is too great, there is a risk that the calculation will not converge. It was therefore tried to target around 0.2 mm of displacement only, between two interruptions to scan the sample by X-ray tomography.

Strain maps obtained by this technique during an interrupted compressive test on a graded scaffold are shown in **Figure B1**. First the highest strain is located in layers made of coarse powder (which are less dense), but in the end, damage appears in the layers containing the two mixed powders. The step after the last one presented here corresponds to the image shown in Figure 8c which highlights a crack in this area.

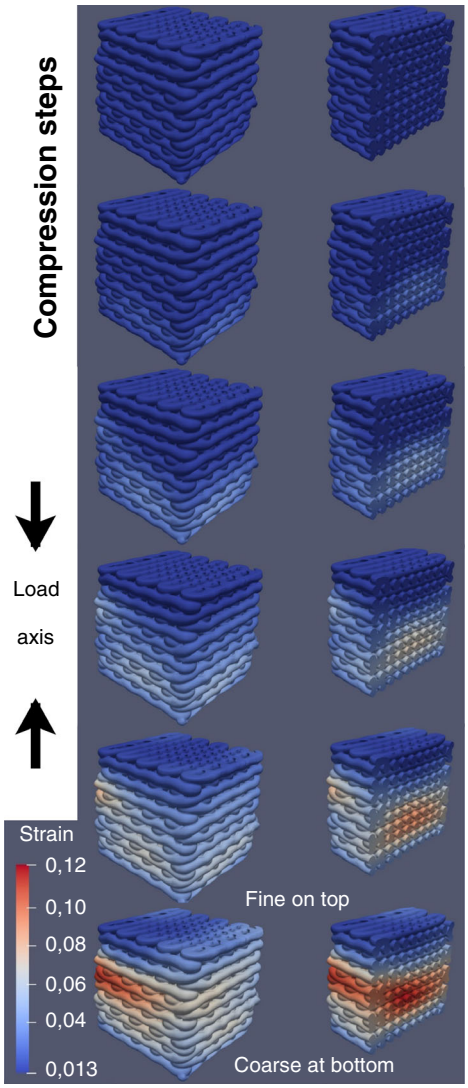

Figure B1. Compression of graded scaffold : strain maps obtained by performing digital volume correlation on X-ray tomographic scans acquired after each step of an interrupted compressive test. First the highest strain is in agreement with layer density then with the location of damage (see Figure 8c).

Acknowledgements

The authors would like to thanks Joël Lachambre for his precious help with Digital Volume Correlation.

Conflict of Interest

The authors declare no conflict of interest.

Author Contributions

M.C: Writing – Original Draft, Investigation, Visualisation. L.G.: Conceptualisation, Supervision, Writing - Review & Editing. X.B.: Conceptualisation, Supervision, Writing - Review & Editing.

Data Availability Statement

The data that support the findings of this study are available from the corresponding author upon reasonable request.

Keywords

additive manufacturing, functionally graded materials, porosity, scaffolds, titanium alloys

Received: August 22, 2022
Revised: October 18, 2022
Published online:

[1] S.-X. Liang, X. Wang, W. Zhang, Y.-J. Liu, W. Wang, L.-C. Zhang, *Appl. Mater. Today* **2020**, *19*, 100543.
[2] L. Tabard, *Appl. Mater. Today* **2020**, *20*, 100658.
[3] B. V. Krishna, S. Bose, A. Bandyopadhyay, *Acta Biomater.* **2007**, *3*, 997.
[4] S. Arabnejad, B. Johnston, M. Tanzer, D. Pasini, *J. Orthopaed. Res.* **2017**, *35*, 1774.
[5] S. Lascano, C. Arévalo, I. Montealegre-Melendez, S. Muñoz, J. A. Rodriguez-Ortiz, P. Trueba, Y. Torres, *Appl. Sci.* **2019**, *9*, 982.
[6] D. M. Robertson, L. St, *J. Biomed. Mater. Res.* **1976**, *10*, 335.
[7] G. Ryan, A. Pandit, D. P. Apatsidis, *Biomaterials* **2006**, *27*, 2651.
[8] N. Taniguchi, S. Fujibayashi, M. Takemoto, K. Sasaki, B. Otsuki, T. Nakamura, T. Matsushita, T. Kokubo, S. Matsuda, *Mater. Sci. Eng. C* **2016**, *59*, 690.
[9] M. Geetha, A. K. Singh, R. Asokamani, A. K. Gogia, *Progr. Mater. Sci.* **2009**, *54*, 397.
[10] Q. Chen, G. A. Thouas, *Mater. Sci. Eng. R: Rep.* **2015**, *87*, 1.
[11] F. Guillemot, *Expert Rev. Med. Devices* **2005**, *2*, 741.
[12] A. H. Glassman, J. D. Bobyn, M. Tanzer, *Clin. Orthopaed. Relat. Res.* **2006**, *453*, 64.
[13] H. A. Zaharin, A. M. Abdul Rani, F. I. Azam, T. L. Ginta, N. Sallih, A. Ahmad, N. A. Yunus, T. Z. A. Zulkifli, *Materials* **2018**, *11*, 2402.
[14] Q. Fu, Y. Hong, X. Liu, H. Fan, X. Zhang, *Biomaterials* **2011**, *32*, 7333.
[15] X. P. Fan, B. Feng, Y. L. Di, J. X. Wang, X. Lu, J. Weng, *Powder Metall. Metal Ceram.* **2012**, *51*, 372.
[16] Y. Chen, D. Kent, M. Bermingham, A. Dehghan-Manshadi, G. Wang, C. Wen, M. Dargusch, *Bioactive Mater.* **2017**, *2*, 248.
[17] S. Wang, L. Liu, K. Li, L. Zhu, J. Chen, Y. Hao, *Mater. Des.* **2019**, *168*, 107643.
[18] R. Scaffaro, F. Lopresti, A. Maio, F. Sutera, L. Botta, *J. Appl. Biomater. Funct. Mater.* **2017**, *15*, 107.
[19] C. Zhu, J. Qiu, S. Thomopoulos, Y. Xia, *Adv. Healthc. Mater.* **2021**, *10*, 2002269.
[20] J. Parthasarathy, B. Starly, S. Raman, A. Christensen, *J. Mech. Behav. Biomed. Mater.* **2010**, *3*, 249.
[21] M. De Wild, S. Zimmermann, J. Rüegg, R. Schumacher, T. Fleischmann, C. Ghayor, F. E. Weber, *3D Print. Addit. Manufact.* **2016**, *3*, 142.
[22] I. Eldesouky, O. Harrysson, H. West, H. Elhofy, *Addit. Manufact.* **2017**, *17*, 169.
[23] V. Karageorgiou, D. Kaplan, *Biomaterials* **2005**, *26*, 5474.
[24] L. Wang, J. Kang, C. Sun, D. Li, Y. Cao, Z. Jin, *Mater. Des.* **2017**, *133*, 62.
[25] C. Han, Y. Li, Q. Wang, S. Wen, Q. Wei, C. Yan, L. Hao, J. Liu, Y. Shi, *J. Mech. Behav. Biomed. Mater.* **2018**, *80*, 119.
[26] E. Onal, J. E. Frith, M. Jurg, X. Wu, A. Molotnikov, *Metals* **2018**, *8*, 200.
[27] L. J. Gibson, M. F. Ashby, in *Cellular Solids: Structure And Properties*, Cambridge University Press, Cambridge, UK **1999**.
[28] K. A. Hing, B. Annaz, S. Saeed, P. A. Revell, T. Buckland, *J. Mater. Sci. Mater. Med.* **2005**, *16*, 467.
[29] S. K. Lan Levengood, S. J. Polak, M. B. Wheeler, A. J. Maki, S. G. Clark, R. D. Jamison, A. J. Wagoner Johnson, *Biomaterials* **2010**, *31*, 3552.
[30] O. Chan, M. J. Coathup, A. Nesbitt, C. Y. Ho, K. A. Hing, T. Buckland, C. Campion, G. W. Blunn, *Acta Biomater.* **2012**, *8*, 2788.
[31] S. J. Polak, L. E. Rustom, G. M. Genin, M. Talcott, A. J. Wagoner Johnson, *Acta Biomater.* **2013**, *9*, 7977.
[32] M. Bohner, G. Baroud, A. Bernstein, N. Döbelin, L. Galea, B. Hesse, R. Heuberger, S. Meille, P. Michel, B. von Rechenberg, J. Sague, H. Seeherman, *Mater. Today* **2017**, *20*, 106.
[33] F. O'Brien, B. Harley, I. Yannas, L. Gibson, *Biomaterials* **2005**, *26*, 433.
[34] R. Cunningham, S. P. Narra, C. Montgomery, J. Beuth, A. D. Rollett, *JOM* **2017**, *69*, 479.
[35] S. Liu, Y. C. Shin, *Mater. Des.* **2019**, *164*, 107552.
[36] Q. C. Liu, J. Elambasseril, S. J. Sun, M. Leary, M. Brandt, P. K. Sharp, *Adv. Mater. Res.* **2014**, *891–892*, 1519.
[37] T. Mukherjee, *J. Manuf. Process.* **2018**, *36*, 442.
[38] M. Bayat, A. Thanki, S. Mohanty, A. Witvrouw, S. Yang, J. Thorborg, N. S. Tiedje, J. H. Hattel, *Addit. Manuf.* **2019**, *30*, 100835.
[39] A. A. Martin, N. P. Calta, J. A. Hammons, S. A. Khairallah, M. H. Nielsen, R. M. Shuttlesworth, N. Sinclair, M. J. Matthews, J. R. Jeffries, T. M. Willey, J. R. I. Lee, *Mater. Today Adv.* **2019**, *1*, 100002.
[40] Z. Jiang, O. Erol, D. Chatterjee, W. Xu, N. Hibino, L. H. Romer, S. H. Kang, D. H. Gracias, *ACS Appl. Mater. Interfaces* **2019**, *11*, 28289.
[41] H. Baniasadi, R. Ajdary, J. Trifol, O. J. Rojas, J. Seppälä, *Carbohydr. Polym.* **2021**, *266*, 118114.
[42] J. I. Cesarano, T. Baer, P. Calvert, Recent Developments in Freeform Fabrication of Dense Ceramics from Slurry Deposition, Technical Report, SAND–97-2857C, CONF-970888–, 554831, **1997**.
[43] J. E. Smay, J. Cesarano, J. A. Lewis, *Langmuir* **2002**, *18*, 5429.
[44] J. A. Lewis, J. E. Smay, J. Stuecker, J. Cesarano, *J. Am. Ceram. Soc.* **2006**, *89*, 3599.
[45] E. Feilden, E. G.-T. Blanca, F. Giuliani, E. Saiz, L. Vandeperre, *J. Eur. Ceram. Soc.* **2016**, *36*, 2525.
[46] B. Y. Ahn, E. B. Duoss, M. J. Motala, X. Guo, S.-I. Park, Y. Xiong, J. Yoon, R. G. Nuzzo, J. A. Rogers, J. A. Lewis, *Science* **2009**, *323*, 1590.
[47] H. Elsayed, P. Rebesan, G. Giacomello, M. Pasetto, C. Gardin, L. Ferroni, B. Zavan, L. Biasetto, *Mater. Sci. Eng. C* **2019**, *103*, 109794.
[48] M. Kachit, A. Kopp, J. Adrien, E. Maire, X. Boulnat, *J. Mater. Res. Technol.* **2022**, *20*, 1341.
[49] B. G. Compton, J. A. Lewis, *Adv. Mater.* **2014**, *26*, 5930.
[50] T. Lin, L.-P. Jin, J.-Y. Yuan, H.-P. Shao, F.-C. Yu, W.-Y. Li, X.-B. He, X. Deng, *Rare Metals* **2021**, *40*, 590.
[51] J. M. Ortega, M. Golobic, J. D. Sain, J. M. Lenhardt, A. S. Wu, S. E. Fisher, L. X. Perez Perez, A. W. Jaycox, J. E. Smay, E. B. Duoss, T. S. Wilson, *Adv. Mater. Technol.* **2019**, *4*, 1800717.
[52] M. A. Skylar-Scott, J. Mueller, C. W. Visser, J. A. Lewis, *Nature* **2019**, *575*, 330.
[53] J. H. Lee, D. J. Won, H. W. Kim, H. J. Park, *J. Food Eng.* **2019**, *256*, 1.
[54] J. Gonzalez-Gutierrez, S. Cano, S. Schuschnigg, C. Kukla, J. Sapkota, C. Holzer, *Mater.* **2018**, *11*, 840.

[55] R. M. German, *Metall. Trans. A* **1992**, *23*, 1455.
[56] I. M. Robertson, G. B. Schaffer, *Powder Metall.* **2010**, *53*, 146.
[57] J. L. Cabezas-Villa, J. Lemus-Ruiz, D. Bouvard, O. Jiménez, H. J. Vergara-Hernández, L. Olmos, *Int. J. Miner. Metall. Mater.* **2018**, *25*, 1389.
[58] M. Coffigniez, L. Gremillard, S. Balvay, J. Lachambre, J. Adrien, X. Boulnat, *Addit. Manuf.* **2021**, *39*, 101859.
[59] A. M'Barki, L. Bocquet, A. Stevenson, *Sci. Rep.* **2017**, *7*, 6017.
[60] R. Landers, A. Pfister, *J. Mater. Sci.* **2002**, *37*, 3107.
[61] J. Schindelin, I. Arganda-Carreras, E. Frise, V. Kaynig, M. Longair, T. Pietzsch, S. Preibisch, C. Rueden, S. Saalfeld, B. Schmid, J.-Y. Tinevez, D. J. White, V. Hartenstein, K. Eliceiri, P. Tomancak, A. Cardona, *Nat. Methods* **2012**, *9*, 676.
[62] T. Persenot, A. Burr, R. Dendievel, J.-Y. Buffière, E. Maire, J. Lachambre, G. Martin, *Materialia* **2020**, *9*, 100589.
[63] M. Coffigniez, L. Gremillard, M. Perez, S. Simon, C. Rigollet, E. Bonjour, P. Jame, X. Boulnat, *Acta Mater.* **2021**, *219*, 117224.
[64] M. F. Ashby, A. G. Evans, N. A. Fleck, L. J. Gibson, J. W. Hutchinson, H. N. G. Wadley, *Metal Foams: A Design Guide* Elsevier, Amsterdam **2000**, p. 263.
[65] R. M. German, in *Particulate Composites*, Springer, New York **2016**.
[66] S.-J. L. Kang, in *Sintering: Densification, Grain Growth and Microstructure*, Elsevier, Amsterdam **2004**.
[67] G. Pyka, A. Burakowski, G. Kerckhofs, M. Moesen, S. Van Bael, J. Schrooten, M. Wevers, *Adv. Eng. Mater.* **2012**, *14*, 363.
[68] T. B. Kim, S. Yue, Z. Zhang, E. Jones, J. R. Jones, P. D. Lee, *J. Mater. Process. Technol.* **2014**, *214*, 2706.
[69] A. Alghamdi, D. Downing, M. McMillan, M. Brandt, M. Qian, M. Leary, *Int. J. Adv. Manuf. Technol.* **2019**, *105*, 1275.
[70] T. Persenot, Doctoral Dissertation, Université de Lyon **2018**.
[71] ThermoTech, TTTI3 Database, http://www.thermotech.co.uk/databases.html#Ti-DATA (accessed: October, 2022).
[72] H. Ledbetter, M. Dunn, S. Kim, R. Fields, in *Void Shape in Sintered Titanium, Review of Progress in Quantitative Nondestructive Evaluation*, **1995**, pp. 1633–1639.
[73] I.-H. Oh, N. Nomura, N. Masahashi, S. Hanada, *Scr. Mater.* **2003**, *49*, 1197.
[74] E. Baril, *PIM Int.* **2010**, *4*, 22.
[75] S. Zabler, *Materials Characterization* **2011**, *62*, 1205.
[76] J. Lachambre, Doctoral Dissertation, Lyon, INSA **2014**.